PAPER • OPEN ACCESS

Cooling rate calibration and mapping of ultra-short pulsed laser modifications in fused silica by Raman and Brillouin spectroscopy

Cooling rate calibration and mapping of ultra-short pulsed laser modifications in fused silica by Raman and Brillouin spectroscopy

Michael Bergler[1,2,3] (ID)**, Kristian Cvecek**[1,3] (ID)**, Ferdinand Werr**[2]**, Martin Brehl**[2]**, Dominique De Ligny**[2] **and Michael Schmidt**[1,3]

[1] Friedrich-Alexander-Universität Erlangen-Nürnberg, Institute of Photonic Technologies, Erlangen, Germany
[2] Friedrich-Alexander-Universität Erlangen-Nürnberg, Institute of Glass and Ceramics, Erlangen, Germany
[3] Friedrich-Alexander-Universität Erlangen-Nürnberg, SAOT – Erlangen Graduate School in Advanced Optical Technologies, Erlangen, Germany

E-mail: michael.bergler@fau.de

CrossMark

Abstract

This paper focuses on the preparation of a new extended set of calibrations of cooling rate (fictive temperature) in fused silica determined by inelastic light scattering and its subsequent use to characterize the local cooling rate distribution in ultra-short pulsed (USP) laser modification. In order to determine the thermal history (e.g. cooling rate and fictive temperature) of fused silica, high-resolution inelastic light-scattering experiments (Raman and Brillouin spectroscopy) were investigated. Calibrations were performed and compared to the existing literature to quantify structural changes due to a change of fictive temperature. Compared to existing calibrations, this paper provides an extension to lower and higher cooling rates. Using this new set of calibrations, we characterized a USP laser modification in fused silica and calculated the local fictive temperature distribution. An equation relating the fictive temperature (T_f) to cooling rates is given. A maximum cooling rate of 3000 K min^{-1} in the glass transition region around 1200 °C was deduced from the Raman analysis. The Brillouin observations are sensitive to both the thermal history and the residual stress. By comparing the Raman and Brillouin observations, we extracted the local residual stress distribution with high spatial resolution. For the first time, combined Raman and Brillouin inelastic light scattering experiments show the local distribution of cooling rates and residual stresses (detailed behavior of the glass structure) in the interior and the surrounding of an USP laser modified zone.

Keywords: glass structure, ultra-short pulsed laser, fused silica, cooling rate, fictive temperature, Raman spectroscopy, Brillouin spectroscopy

Some figures may appear in colour only in the online journal

1. Introduction

The processing of glass with ultra-short pulsed (USP) lasers for cutting [1], ablating, welding [2] or modifying, on the surface as well as inside the volume [3], is a well-researched topic with the potential for novel applications [4]. The localized modification in the physical and chemical properties of transparent media allows various applications, such as photonic, microfluidic and micro mechanical devices. A better understanding of photonic applications, like direct waveguide writing in transparent media, presents the possibility for improvements in the communication sector [5]. Industrial processes use USP laser for surface polishing or 'finishing' to achieve specific roughness requirements [6]. In the medical sector, the internal modification and subsequent selective etching of the laser-modified zone generates specific geometries of microfluidic devices used in merging lab-on-a-chip devices [7]. The final properties of the laser-modified zones depend on the pulse duration, average power, pulse repetition rate and feeding speed which affect the physical conditions present during the laser-glass interaction such as temperature and pressure in glass media [8]. As a result, the irradiation conditions used during the modification process ultimately determine the network structure.

The localized change of properties, (i.e. density and refractive index) is based on rearrangements of the glass network which is influenced by the cooling rate and residual stress within the medium [9]. Cooling rate and residual stress affect the atomic structure of glass. To understand how either cooling rate or residual stress effect the behavior of the glass network, it is necessary to analyze both effects separately [10]. This has been done for residual stress with isostatic or uni-axial compression and monitoring the response of the glass network *in-situ* or after treatment at a certain pressure (often in the range of several gigapascal) [11–13]. In order to assess the effects of different cooling rates, glass is heated well above the glass transition temperature (T_g) and cooled at a set cooling rate using a differential scanning calorimeter (DSC) or a conventional annealing process [14, 15].

Since it is not always possible to monitor or determine the cooling rate of a glass, the fictive temperature (T_f) is used to describe the thermal history of a glass. During the cooling process, the viscosity of a glass-forming material increases as the temperature decreases until the glass-forming material can no longer adjust to the low temperature state. At this point, the material transitions from its liquid state and into a frozen, non-equilibrium (glassy) state [16]. In the glass transition range, the T_f is thermodynamically defined as the point at which the enthalpies of the solid (glassy) and the liquid states intersect. Since this is a time-dependent process, T_f depends on the cooling rate. A fast cooling rate leads to a high T_f, and conversely, a slow cooling rate to a low T_f. This fact is used in conventional annealing processes where glass is heated at certain temperatures in the glass transition range, relaxed and subsequently quenched in water. The relaxation time of the glass structure (i.e. the time required to reach an equilibrium state in the network) depends on the viscosity of the glass at a specific temperature [17]. This results in shorter relaxation times for materials with lower viscosity and longer relaxation times for highly viscous materials. If the glass is fully relaxed at a certain temperature and then quenched significantly faster than the relaxation time, the T_f of that glass is its annealing temperature [18]. For example, using faster cooling rates in fused silica yields denser glass structures.

We used fused silica in our study since most commercial glass is silica-based and the glass structure is thus not affected by network modifying additives. To find the physical conditions at which the glass was modified, we used the so called 'memory effect' of the thermal history of the glass network [18]. This means, the glass network changes according to the applied pressure, cooling rate or radiation and can be analyzed afterwards.

We analyzed different cooling rates observing T_f with inelastic light scattering, Raman, and Brillouin spectroscopy. Different calibration methods linking these spectroscopies to T_f were already reported for fused silica in the literature at a small temperature range around T_g (1200 °C). New samples of fused silica were equilibrated at different T_f by the annealing method. As shown in section 3, we expanded the relationship between cooling rate and fictive temperature to include lower and higher cooling rates than those reported in existing literature. The new calibrations obtained were extrapolated and used to evaluate the behavior of extremely high cooling rates matching the conditions encountered after USP laser modification. A modified zone was inscribed with 3 W average power, 2 MHz repetition rate, and 200 mm s^{-1} feeding speed and was mapped at high spatial resolution using inelastic light scattering. The optical and acoustic responses of the modified glass structure was evaluated before the local T_f distribution was estimated [19]. The local cooling rates were calculated by relating the T_f distribution to the viscosity of fused silica. Comparing the observations obtained from Raman spectroscopy to the Brillouin analysis, we determined the local residual stresses caused by the USP laser modification.

2. Experimental procedure and methods

The fused silica used in the experiments (specification EN08) were electrically molten natural quartz glass with a SiO$_2$ content above 99.98% and a hydroxyl content below 150 ppm. A complete chemical characterization is listed in [20]. The glass samples were 1 mm thick with both sides polished to optical standards.

2.1. Correlation of fictive temperature to the cooling rate

One way to evaluate the cooling rate (q_g) in the temperature domain of the glass transition, is to determine the T_f, at which structural relaxation does not have enough time to take place. When the liquid is taken as a Maxwell body, its relaxation time (τ_r) is related to the shear modulus (G_∞) and the viscosity (η) by the following relation:

$$\tau_r = \frac{\eta}{G_\infty} \tag{1}$$

Furthermore, following [21–23], T_f can be directly related to q_g using the viscosity–temperature dependence with:

$$\log\left(q_g\left(T_f\right)\right) = 13 - \log\left(\eta\left(T_f\right)\right)$$
$$= 13 - A + \frac{B}{\left(T_f - T_0\right)} \quad (2)$$
$$= -5.66 + \frac{19433}{\left(T_f - 364.15\right)}$$

where q_g will be in K/min, η in Pa · s, T_f and T_0 in K. The three variables A, B and T_0 are the traditional coefficients of the Vogel–Fulcher–Tammann (VFT) equation. The numerical values reported in the equation above were obtained from the SciGlass database.

2.2. Calibration of fictive temperature to vibrational spectra

Isothermal treatment is an effective method for preparing calibration samples with different T_f. Isothermal treatment was performed by placing the glass sample inside a platinum crucible within an annealing furnace, which was kept at the desired T_f. The annealing time was chosen to be longer than the relaxation time τ_r and calculated using equation (2). The samples were kept in the annealing furnace three times longer than the τ_r ($3 \cdot \tau_r$). After annealing, the samples were quenched in direct contact using distilled deionized water to ensure fast cooling. If the cooling time (the duration of the quenching procedure) at the end of the isothermal treatment is significantly shorter than the relaxation time, the prepared glass samples will have the desired fictive temperature T_f— which equals the annealing temperature.

In this way, samples with T_f ranging from 990 °C to 1250 °C were prepared. The corresponding cooling rates (in the domain of the glass transition) range from 0.001 K min^{-1} to 78 K min^{-1}. Using distilled deionized water at room temperature yielded a short quenching duration (t < 1 s) and prevented further relaxation. Compared to previous studies, using the calibrations reported in this paper, we obtained samples with lower T_f ranges than those reported in previous studies.

We prepared three other samples at 1300 °C, 1350 °C and 1400 °C, as reported in previous studies. At these high temperatures, the cooling rates necessary to obtain the corresponding T_f is above 390 K min^{-1} and thus too high to be achieved under typical quenching conditions [17]. These samples did not maintain the desired T_f. The observations from these three samples appear in red on the calibration curves. These observations were excluded from the fit (see figures 1 to 4) to avoid overestimating T_f by quenching the calibration samples not fast enough. The temperature ranges used in previous studies reported in literature are represented in figures 2 to 4 as blue dashed lines. All of the compared studies observed temperatures that far exceeded 1250 °C—the highest temperature reported in our experiments. This discrepancy explains why our calibrations show a larger slope than the literature values. Indeed, our results showed a similar slope after fitting our observations in the temperature interval reported in previous literature and including results for samples with high T_f. The
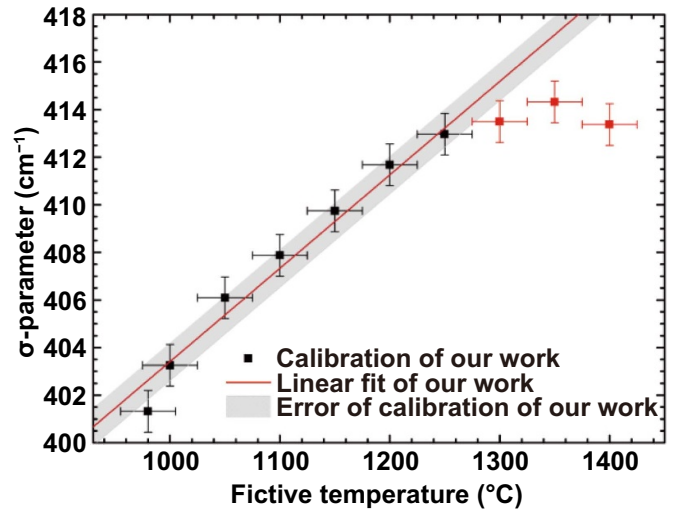

Figure 1. Evaluation of the σ-parameter calculated from the Raman spectra of the calibration samples. The σ-parameter takes the wavenumber region from 150 to 690 cm^{-1} into account. The observed shift (black points) of the σ-parameter is linearly fitted (red line) from 980 °C to 1250 °C, excluding 1300 °C–1400 °C (red points) due to uncertainties in the production process. Error interval of the calibration is shown as a grey background.
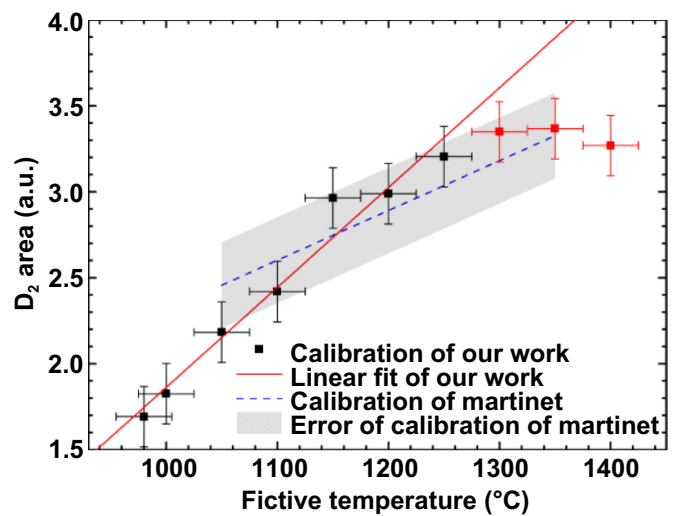

Figure 2. Raman spectrum evaluated for the area of the D$_2$ band after baseline correction and normalization to the total area. The symbols (black points) indicate the observations of our work including a linear fit (red line) of the data from 980 to 1250 °C, excluding the data from 1300 to 1400 °C (red points) due to uncertainties in the production process. The blue dashed line shows the previous literature calibration, the interval used for the fit as well as the error as a grey background.

error of the fit reported in literature is represented as a grey background in figures 1–4.

The calibration samples subjected to different cooling rates were characterized with vibrational spectroscopic analysis methods, which observed both the acoustic vibrations (*Brillouin shift*) and optical vibrations (Raman shift) at room temperature.
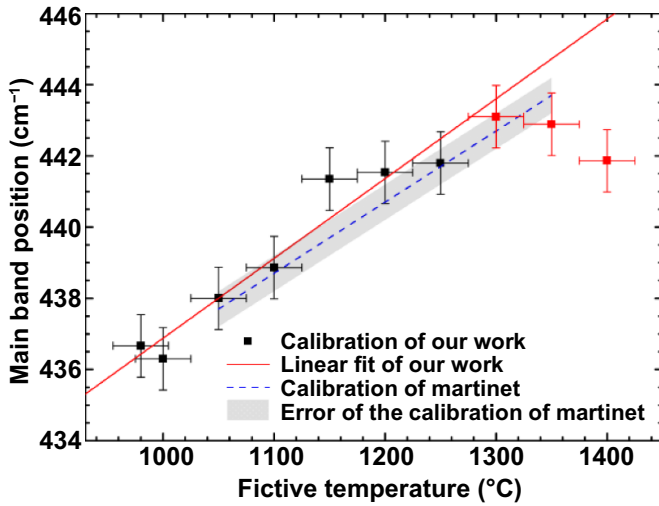
Figure 3. Evaluation of the main band position calculated from the Raman spectra. The symbols (black points) indicate the observations of our work including a linear fit (red line) of the data from 980 °C to 1250 °C, excluding the data from 1300 °C to 1400 °C (red points) due to uncertainties in the production process. The blue dashed line shows the previous literature calibration, the interval used for the fit as well as the error as a grey background.
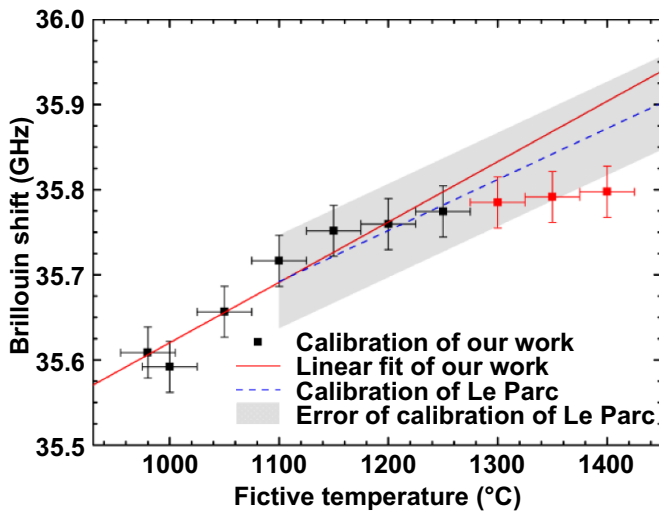

Figure 5. Example of Raman spectra of fused silica EN08 displayed with different cooling rates ranging from slow-cooled (obtainable with conventional annealing methods) to fast- and extreme-fast-cooled (obtained after ultra-short pulsed laser irradiation). 2.3.1 explains the assignment of the different bands in the spectra above. The inset shows the raw Raman signal (black) for the slow-cooled sample with the fourth order polynomial baseline (red) applied for background correction.

Figure 4. Brillouin spectrum evaluated for the average shift position of the signal. The symbols (black points) indicate the observations of our work including a linear fit (red line) of the data from 980 °C to 1250 °C, excluding the data from 1300 °C to 1400 °C (red points) due to uncertainties in the production process. The blue dashed line shows the previous literature calibration, the interval used for the fit as well as the error as a grey background.

2.3. Vibrational analysis

The vibrational analysis was performed with the in-house built ARABICA (Associated Raman Brillouin Calorimeter) spectrometer [24]. A single frequency 488 nm CW laser source (coherent sapphire SF) was used to excite optical and acoustic vibrations inside the glass network at the laser focal point. For further description purposes we will refer to this laser as Raman–Brillouin analysis (RBA) laser. In a 180° reflective
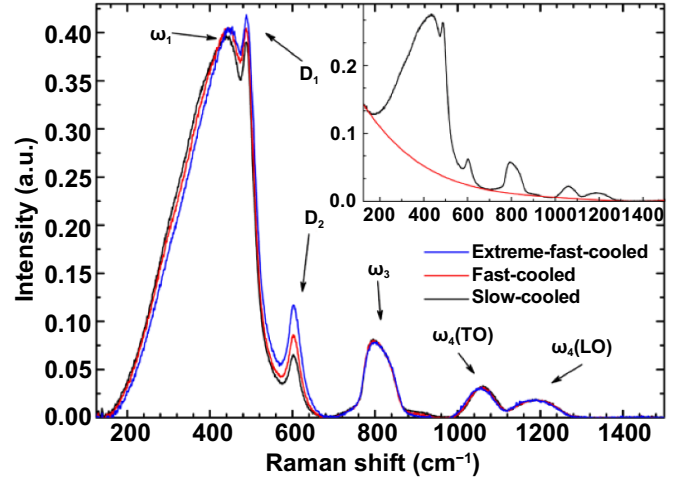
measurement setup the scattered light contains the Rayleigh (elastically scattered light), the Raman (optically scattered light) and the Brillouin (acoustically scattered light) contributions. The Brillouin signal was observed using a tandem Fabry–Perot interferometer (TFP). The Raman signal was analyzed with a CCD camera after passing a monochromator with a high spectral resolution grating. The exact technical specifications as well as a precise description of the setup was published by Veber *et al* [24]. Combining a focusing objective (NA 0.42, WD 20.5 mm) with a three-axis stage assembly allows scanning of large 2D areas.

Our work focuses on four different observables for the vibrational analysis. Three observables were obtained from the Raman signal: the σ-parameter (1st observable), the *main band position* (2nd observable) and the *D_2 area* (3rd observable). The fourth observable was the *Brillouin shift*.

2.3.1. Raman spectroscopy.
An example of Raman spectra of fused silica EN08 subjected to different cooling rates is shown in figure 5. The slow-cooled sample was obtained with a conventional annealing method at a cooling rate of 10 K min^{-1}. The fast-cooled and extreme-fast-cooled samples were produced via USP laser irradiation and a subsequent rapid quenching effect of the surrounding cold-glass network. In contrast to Deschamps *et al*, we baseline corrected our spectra using a fourth order polynomial baseline with anchor points at 145, 685, 975, 1460 cm^{-1} and normalized to the total area of the spectrum (total area = 100) [12]. Combining a fourth order polynomial baseline with the chosen anchor points achieved a highly stable fit for all treated spectra. The inset in figure 5 shows a raw spectrum of the slow-cooled sample with the associated fourth order baseline as background correction.

The displayed spectra show typical bands for amorphous SiO_2 previously described in the literature. The so-called 'main band' (ω_1), around 445 cm^{-1}, is associated with the intertetrahedral Si-O-Si bond angle distribution. With increasing cooling rate, the band broadens and shifts to higher frequencies resulting in a decrease of the mean Si-O-Si bond angle and a widening of the distribution [25]. D_1 at 490 cm^{-1} and D_2 at 605 cm^{-1} are assigned to 4- and 3-membered SiO_4 defect rings, respectively. These ring structures appear sensitive to permanent densification [12, 13], residual stress [26], cooling rate [27], and irradiation. All these phenomena induce a general rearrangement of the network structure [28, 29]. ω_3 and ω_4 can be found in the literature and will not be further discussed in our work [30]. All spectra were collected in a wavenumber range from 50 to 1450 cm^{-1}. No vibrational contributions of the glass network of fused silica were present above the observed range.

In our work, we focused on a spectral range from 150 to 700 cm^{-1} because this range shows the strongest influence on structural rearrangements compared to the relatively small changes in ranges exceeding 700 cm^{-1}. Changes of the main D_1 and D_2 bands were integrated to determine the σ-parameter defined by Deschamps *et al* [12] (see equation (3)).

$$\frac{\int_{\alpha 1}^{\sigma} I_{Raman}(\alpha)\,d\alpha}{\int_{\alpha 1}^{\alpha 2} I_{Raman}(\alpha)\,d\alpha} = \frac{1}{2}. \tag{3}$$

Equation (3) describes the σ-parameter (1st observable) with $\alpha 1$ as the lower border of the integral (in our work set to 150 cm^{-1}) and $\alpha 2$ as the higher border of the integral (in our work set to 690 cm^{-1}). The *position of the main band* (2nd observable) peak was calculated at the maximum intensity of the ω_1 band. The main band was fitted by a fourth order polynomial between 380 and 430 cm^{-1} to denoise the spectrum and minimize the calculation error. The D_2 *area* (3rd observable) was calculated between 570 and 650 cm^{-1}. All observables were calculated after baseline correction and normalization to the total area of the spectrum.

2.3.2. Brillouin spectroscopy. Figure 6 contains examples of Brillouin spectra. The incident laser on the measured sample interfered with the acoustic vibrations parallel to the incident laser (z-direction). The observed signal (*Brillouin shift*) represents the diffracted portion of the incident RBA laser at the wave fronts of the induced vibrations, which correlate with the sound velocity of the observed material. The shown Brillouin shifts and Raman measurements were collected simultaneously. The displayed spectra in figure 6 for slow-, fast- and extreme-fast-cooled glass show both negative (anti-Stokes signal) and positive (Stokes signal) Brillouin shifts. Due to experimental restrictions, the arithmetic mean value of the anti-Stokes and Stokes signal was calculated to determine the *Brillouin shift* (4th observable). A rearrangement in the network structure due to difference in pressure or cooling rate, alters the Si-O-Si bond angle distribution. The change of the bond angle distribution modifies the sound velocity of the glass network, and therefore, induces a shift in the observed Brillouin signal [13].
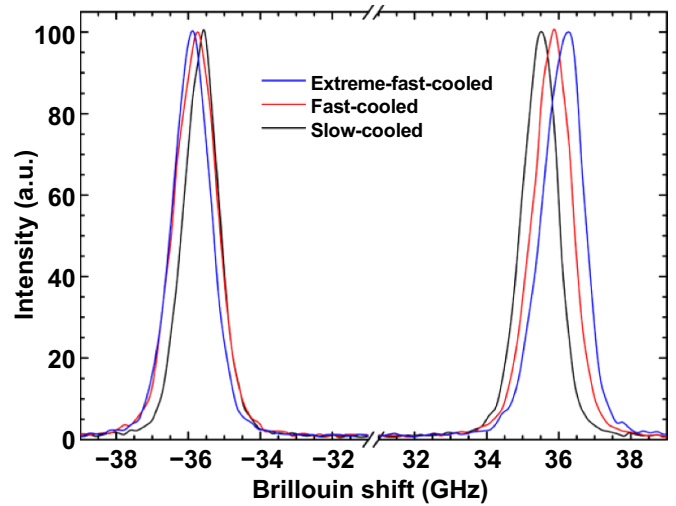

Figure 6. Example of Brillouin spectra of fused silica EN08 displayed with different cooling rates ranging from slow-cooled (obtainable with conventional annealing methods) to fast- and extreme-fast-cooled (obtained after ultra-short pulsed laser irradiation). Negative shifts are related to the anti-Stokes signal (left) and positive shifts to the Stokes signal (right) respectively.
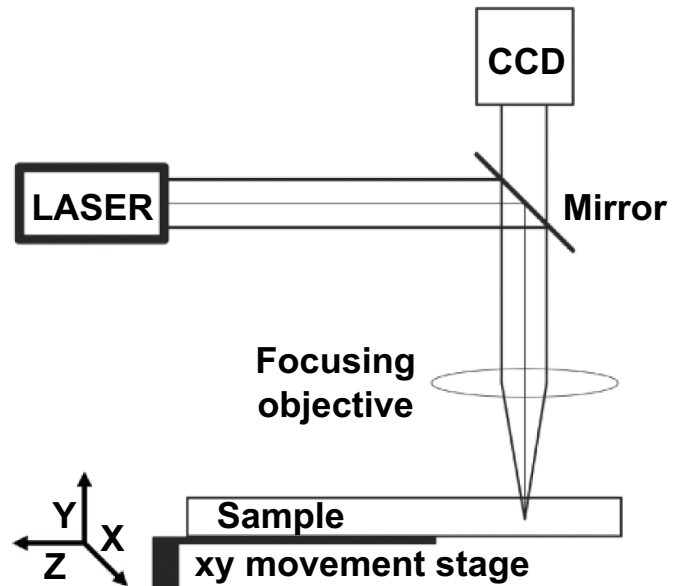

Figure 7. Schematic representation of the experimental setup used for the USP modification process. The sample surface is aligned perpendicular to the incident laser using the CCD camera.

2.4. Ultra-short pulsed laser modification

The glass modification experiments in our work were performed using a mode-locked Nd:YVO_4-laser (Fuego, Time-Bandwidth Products, Switzerland). This system emits pulses with a FWHM-duration of 10 ps at 1064 nm wavelength with an adjustable repetition rate from 50 kHz to 8 MHz and a nominal average output power up to 30 W. In our work, the repetition rate was set to 2 MHz and the output power was set to 3 W (see [31]).
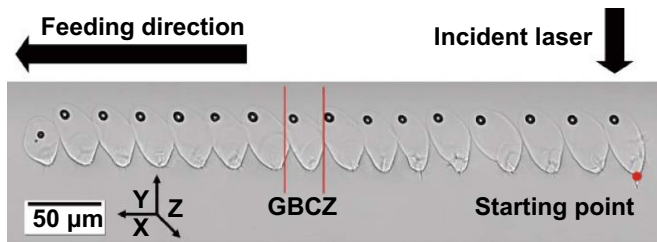
Figure 8. Optical image of a laser modified zone inscribed perpendicular to the viewing direction from right to left with the incident laser from above (y-direction). Used laser parameters: 3 W average power, 2 MHz repetition rate, 200 mm s^{-1} feeding speed. The red dot marks the starting point of the USP laser generating the shown modified zone. The red box indicates a molten zone referred to as gas bubble cycle zone (GBCZ).

The laser was focused using a wavelength corrected ELWD microscope objective with a numerical aperture (*NA*) of 0.7 and a correction collar to compensate for spherical aberrations and to achieve a focus-depth independent focal spot size. A schematic representation of the setup used for the internal USP laser modification is provided in figure 7. The USP laser was incident from above (y-direction) and focused into the volume of the sample. The laser focal spot remained in a fixed position and the fused silica sample was moved along the *x*-axis at a constant speed (200 mm s^{-1}). The acceleration and deceleration occurred outside of the sample to ensure constant irradiation conditions during the modification process.

For all samples, the focal spot was set to a depth of 250 μm below the surface. A correction of the focusing depth due to the refractive index of fused silica ($n = 1.4496$ at 1064 nm [32]) as well as an adjustment of the correction collar of the focusing objective was incorporated.

The laser modified sample from figure 8 was mapped in an *x-y* direction. The mapping depth (*z*-direction) was chosen to be directly in the center of the modified zone. Since the gas bubbles are located in the center (*z*-direction), they were used to place the focal spot of the RBA laser on this plane. This is done using reflections from the generated gas bubbles. The modified zones were mapped with an RBA laser with a focus diameter of 1.4 μm and a step size of 2.5 μm. The entire area was mapped with a total of 20×30 measurement points.

3. Results and discussion

The inscribed modification was optically analyzed to evaluate the lateral behavior of the inscribed modification (figure 8). The focal point of the laser beam induces dynamic plasma formation, which grows quasi-periodically in the direction of the incoming laser [33, 34]. The complete heat-affected zone (HAZ) is visible by a slight change of the refractive index between the unmodified glass and the modified zone. In the upper part of the modified zone, a gas bubble (black dot in figure 8), typical for fused silica but also observed in Borofloat 33 glass types, is generated. This due to agglomeration of smaller bubbles generated during the plasma state of the modification process near the focal spot of the USP laser.

During the process the bubbles are trapped within the laser-plasma-interaction mechanism and dragged in the direction of the moving USP laser [35]. During USP laser modification process, fused silica reaches temperatures between 3000 °C and 4000 °C [34], forming gaseous SiO_2 inside the molten area. The rapid dissociation of gaseous SiO_2 into silicon and oxygen forms the bubbles [35]. At a high feeding speed (e.g. 200 mm s^{-1}), the quasi-periodic plasma motion generates separate molten zones along the feeding direction (*x*-direction) (see figure 8). For description purposes, we will refer to one such cycle (see red box in figure 8) generated during this process as the 'gas bubble cycle zone' (GBCZ).

Using a feeding speed of 200 mm s^{-1} (see figure 8), single GBCZs along the moving direction of the laser are visible. All GBCZs were tilted in the feeding direction (*x*-direction) of the USP laser. The formation of these GBCZs occurred in the following manner: The initial laser pulses ionize the glass network by multi-photon absorption, inciting plasma formation. Inside the plasma, SiO_2 begins dissociating into its component elements. This process forms small oxygen bubbles that agglomerate and move towards the incoming laser beam (y-direction). The laser beam drags the bubbles which are agglomerating inside the plasma along with the plasma (against the motion of the sample) due to a thermal gradient effect described in [36]. With increasing size, the agglomerating bubbles start to block the incident laser beam partially up to a point where the incident energy is no longer sufficient to ionize the network causing the plasma to be extinguished and, consequently, to stop the thermal accumulation in the modification area [34, 35]. Cooling the network increases the viscosity of the glass, freezing the bubble in place. Due to the constant feeding speed, the laser focal spot moves past the blocking bubble, and the described process restarts. For the process parameters used in figure 8 of 3 W average power, 2 MHz repetition rate and 200 mm s^{-1} feeding speed, the average length of a separated structure is 26.36 μm with 10 pulses per μm. At the starting point of the USP laser, the GBCZ shows the formation of randomly distributed cracks.

This defect formation can be attributed to high internal pressure at the initial plasma formation working against a cold and brittle material [31]. For modified zones at high repetition rates or fast feeding speeds—which generate the GBCZs—a defect formation at the focal spot is visible for every GBCZ, because with quasi-periodic laser-plasma-interaction each new GBCZ is generated in yet unmodified and still cold and thus brittle material.

3.1. Fictive temperature calibration curve with a conventional annealing method

A diagram of the σ-parameter depending on T_f is shown in figure 1. The σ-parameter was calculated for the spectral range from 150 to 690 cm^{-1}, as described in 2.3.1. The σ-parameter increases monotonically with T_f from 980 °C to 1250 °C. This T_f range was linearly fitted, excluding values above 1250 °C, as shown in figure 1. It appears impossible to generate higher cooling rates with our conventional annealing method (section 2.2) due to the handling times of the sample

and the short relaxation times (below 1 s) of the glass network above 1250 °C [36]. For calibration purposes, our conventional annealing method limited the obtainable cooling rates; therefore, we excluded results obtained at a T_f above 1250 °C. Data using the σ-parameter for T_f calibration has not been previously reported. As a result, we could not make a direct comparison between our calibration and those reported in the literature.

The following fit equation of our calibration correlates T_f to the σ-parameter. The relationship is valid in a stress regime from 0 to 1 GPa.

$$T_f(^{\circ}C) = \frac{\sigma\left(cm^{-1}\right) - 361 \pm 3\left(cm^{-1}\right)}{0.041 \pm 0.003 \left(\frac{cm^{-1}}{^{\circ}C}\right)}. \tag{4}$$

The observation of the D_2 band area of our work is shown in figure 2 and compared to the results of Martinet *et al* [37]. The evolution of the D_2 *area* shows a monotonical trend with increasing T_f in the temperature range from 980 °C to 1250 °C. Including the new observations in the low T_f range (980 °C and 1000 °C) and considering only the results which are not limited by our conventional annealing method (e.g. below 1250 °C), a different evolution of the D_2 *area* is visible compared to literature. The linear behavior reported in the literature underestimates the T_f. If the results of our work are fitted in the same T_f range reported in the literature, the prediction of the T_f is similar. We expected reliable observations from the low T_f range due to the long relaxation times (>3 h) of the glass network in the sub T_g range (<1200 °C) [38].

The following fit equation of our calibration correlates T_f to the D_2 *area*—abbreviated as D_2 in the equation—after a normalization to the total area of the spectrum (total area = 100). The relationship is valid in a stress regime from 0 to 1 GPa.

$$T_f(^{\circ}C) = \frac{D_2 - 3.9 \pm 0.4}{0.0058 \pm 0.0003 \left(\frac{1}{^{\circ}C}\right)}. \tag{5}$$

The observation of the main band position of our work is shown in figure 3 and compared to the calibration done by Martinet *et al* [37]. The *position of the main band* behaved monotonically with increasing T_f. Our fit considers the range from 980 until 1250 °C. Our calibration and the reported data from literature show a similar behavior with T_f in the observed temperature range.

The following fit equation of our calibration correlates T_f to the main band position (MB). The relationship is only valid in ambient pressure conditions.

$$T_f(^{\circ}C) = \frac{MB\left(cm^{-1}\right) - 414 \pm 3\left(cm^{-1}\right)}{0.022 \pm 0.003 \left(\frac{cm^{-1}}{^{\circ}C}\right)}. \tag{6}$$

As for the Raman observables, the *Brillouin shift* was evaluated using the same T_f range from 980 °C to 1250 °C. The *Brillouin shift* exhibited a linear behavior. Our new calibration deviates only slightly from the prediction of literature [39].

The following fit equation of our calibration correlates T_f to the Brillouin shift (BR). The relationship is only valid in ambient pressure conditions.

$$T_f(^{\circ}C) = \frac{BR\left(GHz\right) - 34.9 \pm 0.1\left(GHz\right)}{0.00071 \pm 0.00009 \left(\frac{GHz}{^{\circ}C}\right)}. \tag{7}$$

The calibration curves reported in previous studies use a different temperature range compared to our study. The range reported by Martinet *et al* [37] (see range of blue dashed lines in figures 2 and 3) observed a temperature range from 1150 °C to 1350 °C. Le Parc *et al* [39] determined the *Brillouin shift* (see range of blue dashed line in figure 4) in a temperature range from 1100 °C to 1450 °C.

Compared to our observed temperature range (980 °C to 1250 °C) the previously reported studies use a significantly higher temperature domain. If our new set of calibration is linearly fitted in the temperature range reported in previous studies, the slope of the linear fit is similar. Therefore, our new set of calibration does not contradict the validity of previous calibrations in their interval of determination. However, our new set of equations should be more reliable in case of extrapolation to hyperquenched (extreme-fast-cooled) glass conditions for the here investigated observables. This is because a T_f calibration procedure at lower temperature domains allows easier and more reliable heat treatment due to the longer relaxation times (τ_r) of the network. This way, undesired but systematic calibration errors that occur in high temperature domains can be excluded. The interval of determination (observed T_f range) plays an important role for the reliability of the calibration curve. An increase in the determination interval could further improve the accuracy of our provided calibrations.

3.2. Extreme-high-cooling rates

For all following observables, the correlating T_f was calculated using the calibrations described above. In figure 9, the evaluation of the σ-parameter is represented by a superposition of the vibrational analysis mapping and the optical microscope transmission image of the modified zone. A T_f of 1150 °C was calculated for the unmodified glass. The glass transformation temperature (T_g, defined for a cooling rate of 10 K min^{-1}) for industrially produced fused silica is 1200 °C [20]. Our observations for the base glass agree with the expected T_f. Significantly higher σ-parameters, correlating with a higher T_f, were observed in the modified zone. The observations increase radially from the edges (1180 °C) to the center (1327 °C). The observations of the σ-parameter of the USP laser modified zone indicate a T_f in the extrapolation range of our calibration method. A maximum T_f was observed in the center of the modified zone indicating a higher cooling rate which can be attributed to higher temperatures during the plasma activity [33, 40, 41]. We expected that heat dissipation via thermal radiation, as opposed to thermal conduction, would have a stronger influence on the cooling rate during the formation of the higher T_f in the center of the modified zone. A stronger contribution of thermal conduction would lead to higher T_f at the edges of the modified zone [37, 42].

The evaluation of the D_2 *area* (see figure 10) shows a T_f distribution similar to the evaluation of the σ-parameter. A T_f
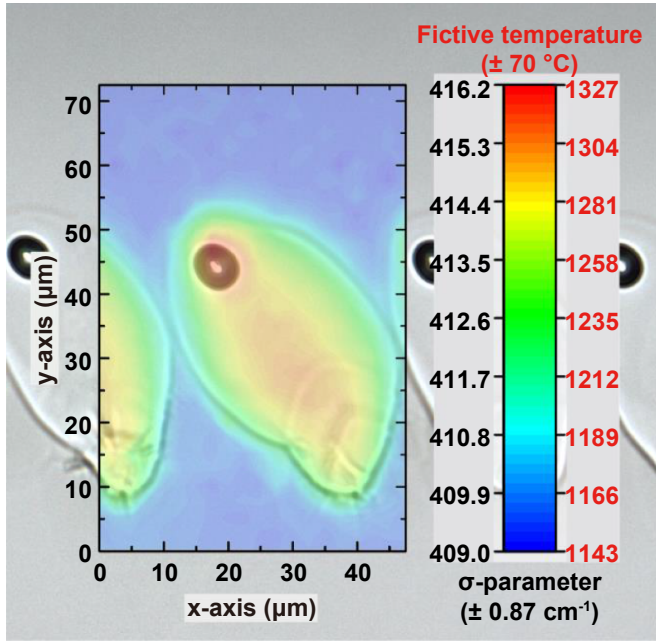
Figure 9. Evaluation of the σ-parameter for a modified zone inscribed with an average power of 3 W, a repetition rate of 2 MHz and a feeding speed of 200 mm s^{-1}. The observed results of the σ-parameter are color coded and overlaid with an optical image of identical scale. Additionally, for the obtained results the T_f was derived from the calibration of our work.
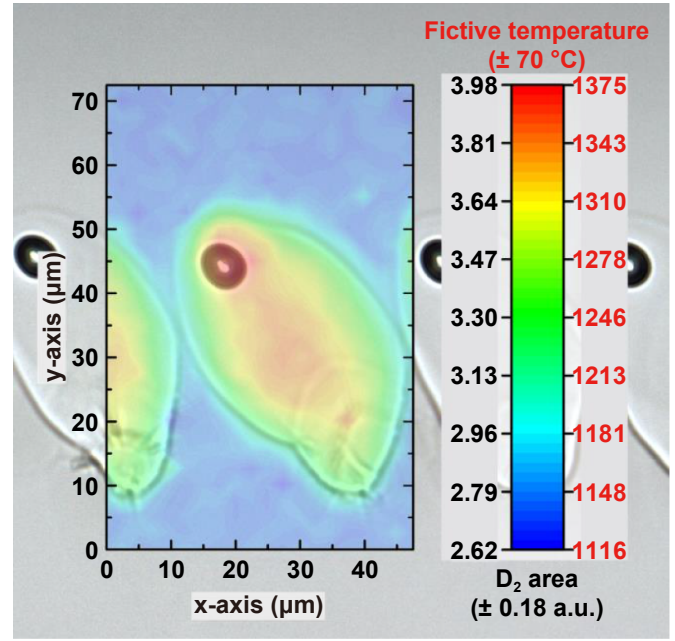

Figure 10. Evaluation of the D$_2$ area for a modified zone inscribed with an average power of 3 W, a repetition rate of 2 MHz and a feeding speed of 200 mm s^{-1}. The observed results of the D$_2$ area are color coded and overlaid with an optical image of identical scale. Additionally, for the obtained results the T_f was derived from the calibration of our work.

of around 1150 °C was calculated for the unmodified glass. The T_f for the modified zone shows a radial increase from the edges (1180 °C) to the center (1375 °C). The maximum T_f was observed at 1375 °C, which corresponds to a cooling rate of 2900 K min^{-1} in the glass transition domain.

Compared to the σ-parameter, the center of the modified zone shows a slightly higher T_f within its error bars. The evaluation methods of the *D$_2$ area* and the σ-parameter show the same T_f distribution for the base glass as well as the modified zone. This can be explained by calculating the σ-parameter (see equation (3)). If the Raman spectra are compared, the biggest change in the range from 150 to 690 cm^{-1} is observable in the increasing D$_2$ band. Neither the main band nor the D_1 band show changes on the same order as the D_2 band with T_f. Therefore, the evolution of the σ-parameter is mainly based on the increase of the D_2 band resulting in similar results for both methods.

The reader might notice that there are some cracks present at the starting points of the GBCZs in figures 8–10. This brings up the question whether or not these cracks have an influence on the Raman observables because they might change the vibrational behavior of optical phonons. As can be seen from the results in figures 9 and 10 either they have no influence on the Raman observables or cannot be resolved with the used evaluation methods.

Compared to the σ-parameter and *D$_2$ area*, the evaluation of the *main band position* (see figure 11) shows a different distribution of the T_f in the modified zone. Compared to figures 9 and 10, no clear pattern-like distribution of the T_f was observed inside the modified zone. Nonetheless, the maximum T_f was
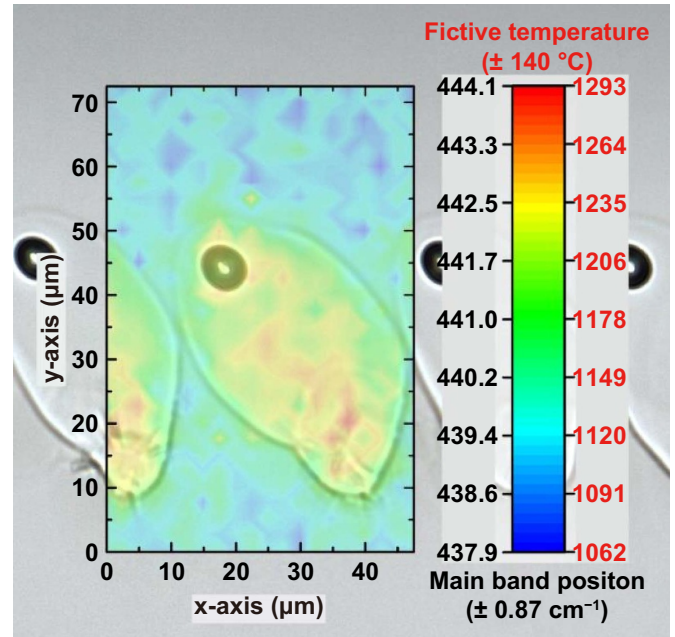

Figure 11. Evaluation of the main band position for a modified zone inscribed with an average power of 3 W, a repetition rate of 2 MHz and a feeding speed of 200 mm s^{-1}. The observed results of the main band position are color coded and overlaid with an optical image of identical scale. Additionally, for the obtained results the T_f was derived from the calibration of our work.

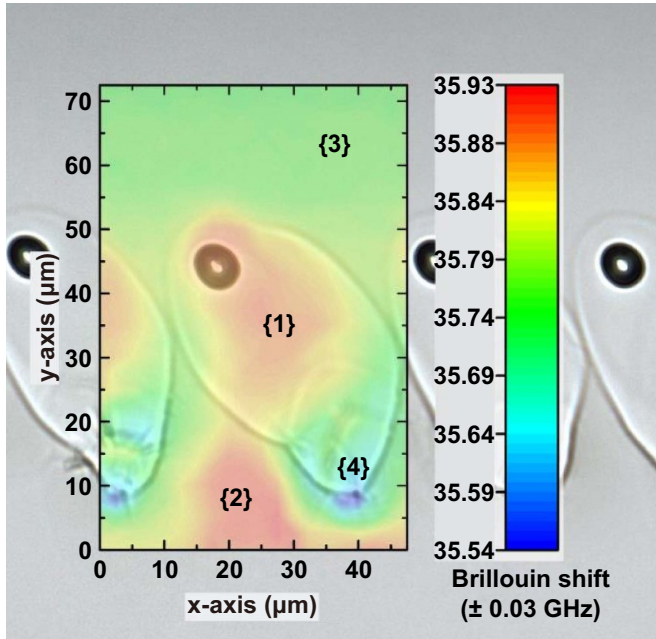visible in both the center of the modified zone and near the focal spot of the USP laser. Compared to the σ-parameter,

Figure 12. Evaluation of the Brillouin shift for a modified zone inscribed with an average power of 3 W, a repetition rate of 2 MHz and a feeding speed of 200 mm s^{-1}. The observed results of the Brillouin shift are color coded and overlaid with an optical image of identical scale. 1 indicates the center of the GBCZ, 2 the region between and below the GBCZ, 3 the unmodified region and 4 the focal area of the USP laser and starting point of the GBCZ.

Figure 13. Correlation of the σ-parameter with the Brillouin shift. The black symbols show the results of our calibration, the red symbols indicate the results of the modified zone. All values of the calibration are linearly fitted (black line). The red line indicates the shifted linear fit of the calibration to fit the results of the modified zone. The difference between the calibration and the modified zone is shown by the blue segment, indicating the residual stress. 1 indicates the center of the GBCZ, 2 the region between and below the GBCZ, 3 the unmodified region and 4 the focal area of the USP laser and starting point of the GBCZ.

the T_f calculated with the *main band position* was generally lower. The maximum T_f calculated for the *main band position* was 1293 °C. Unfortunately, the precision of our calibration function (see figure 3) and our measurement of the *main band position* limits our possible interpretations. The evaluation of T_f using the σ-parameter or D_2 *area* is better than using the *main band position*. Moreover, *in-situ* high pressure experiments have shown that both the σ-parameter and the D_2 *area* are virtually unaffected by pressure up to 1 GPa [43]. Therefore, we can assume that figures 9 and 10 give the purely thermal response of the glass structure.

Figure 12 shows the evaluation of the acoustic vibrations, the *Brillouin shift*. The *Brillouin shift* indicates a different behavior compared to the Raman observations. The *Brillouin shift* in the GBCZ (1 in figure 12) as well as in the area below, (2 in figure 12) shows very high values of up to 35.9 GHz. The unmodified base glass 3 has an intermediate value of 35.75 GHz. Finally, the starting point of the GBCZ 4 shows a lower shift down to 35.5 GHz. The direct application of our calibration (see equation (7)) contradicted the values obtained from the Raman calibrations. The maximum T_f (1442 °C) occurred in the unmodified zone 2, while the lowest cooling rate would have been predicted in zone 4, where the plasma initiation took place. Only zone 3, with a T_f of 1150 °C, was similar to the results of the σ-parameter and the D_2 *area*. After careful observation, the area under the laser focal spot (zone 4) presents microscopic cracks, visible as fringes in the optical image, as well as possible nanobubbles. The cracks are likely
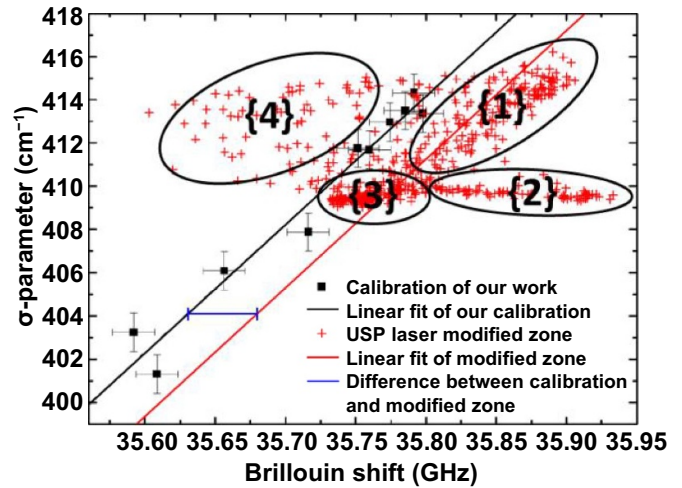
a result of the shockwave formation induced by the incident USP laser on the cold and brittle base glass [44].

The cracks and the possibly inherent nanobubbles can lower the density and the sound velocity of the network, resulting in a lower *Brillouin shift* compared to the unmodified glass.

Conversely, only the existence of residual stress can influence the *Brillouin shift* and modify its dependence on T_f. As Sonneville *et al* [11] reported, using *in-situ* Raman and Brillouin spectroscopy, the *Brillouin shift* decreases under pressures up to 2 GPa. The *Brillouin shift* shows increases in the tensile regime [11]. In the same pressure interval, the Raman spectra of fused silica remains unchanged [43]. The observed *Brillouin shift* at the USP laser focal spot could be interpreted as compressive stress that is not detectable by Raman spectroscopy. The *Brillouin shift* of the modified zone 1 can be attributed to the change in T_f present in the Raman observables. The *Brillouin shift* of the USP laser focal area 4 observes both the thermal history effect and compressive stress linked to the crack formation. No change of T_f was expected in the surrounding of the modified zone (zone 2) due to the absence of thermal accumulation. However, volume variation of nearby GBCZ could have induced a local gradient in the stress distribution between 4 and 2, resulting in tensile stress in 2.

From the Raman observables, we expected a T_f change in the modified area with no influence on the surrounding base glass. The observed *Brillouin shift* indicates the change of T_f with additional influences due to residual stress. By correlating the σ-parameter to the *Brillouin shift*, it is possible to separate the influence of T_f from the influence of pressure (residual stress). The correlation of the σ-parameter with the *Brillouin*

shift as well as the calibration results are shown in figure 13. The different areas defined in figure 12 are also reported. The observations for the unmodified base glass above the GBCZ 3 show almost no variation in both the *Brillouin shift* and the σ-parameter. However, area 2 shows a strong variation in the *Brillouin shift* at constant σ-parameter, indicating a pure stress induced behavior. The results for the modified zone are visible in 1, showing a linear behavior between the *Brillouin shift* and the σ-parameter. The linear fit (red line) of this zone is parallel to our calibration curve (black line) by an offset of $+0.05$ GHz (see blue segment). This indicates that area 1 is predominantly affected by a gradient of the fictive temperature effect, but that it is under low, constant tensile stress. It is in this area where the highest T_f was observed. At the starting point of the GBCZ 4, non-linear changes occurred in both the *Brillouin shift* and the σ-parameter. A combined influence of compressive stress and T_f was observable since the results show higher σ-parameter (correlated only to T_f) and smaller *Brillouin shifts* (correlated to the compressive stress) at the same time. The high scattering of the points in area 4 can be easily explained by the presence of cracks.

As exemplified in area 1, it is possible to differentiate the cooling rate effects from residual stress effects by comparing the Raman signals to the *Brillouin shift*. Sonneville *et al* reported a pressure dependence of the *Brillouin shift* of -2.5 GHz GPa^{-1} [11]. The offset of $+0.05$ GHz corresponds to a tension of 20 MPa. This can be generalized to every point of our mappings. By subtracting the T_f contribution obtained from the σ-parameter from the global *Brillouin shift* (containing the contribution of T_f and residual stress) only the contribution of the residual stress (*RS*) was extracted. The residual stress expressed by the *Brillouin shift* (in GHz) can be quantified in GPa using the aforementioned calibration [11]. A residual stress calibration is given as follows:

$$
\begin{aligned}
&RS\,(GPa)\\
&= \frac{BR\,(GHz) - 0.0173\,\left(\frac{GHz}{cm^{-1}}\right) \cdot \sigma\,(cm^{-1}) - 28.6\,(GHz)}{-2.5\,\left(\frac{GHz}{GPa}\right)}.
\end{aligned}
$$

(8)

Applying this calibration, a residual stress map shown in figure 14 was obtained. Excess stresses were observed at the focal spot of the USP laser and along some of the discontinuities visible at the bottom of the GBCZ, which are probably cracks. The tensile regions are poorly defined as they were defused between and below the GBCZ.

The above-mentioned combination of T_f and residual stresses on the *Brillouin shift* may not completely cover the whole picture. As is reported in the literature, high-energy particles (x-ray photons, electrons, ions) also lead to changes in the Raman spectra without any additional mechanical stress or heat input [28, 29, 45]. USP laser interaction with plasma produces fast electrons that generate x-ray photons [46]. While the laser peak fluence used in our experiments was not as high as in [46], we cannot completely exclude the potential effects electrons, in the laser-generated plasma, have on structural network changes.
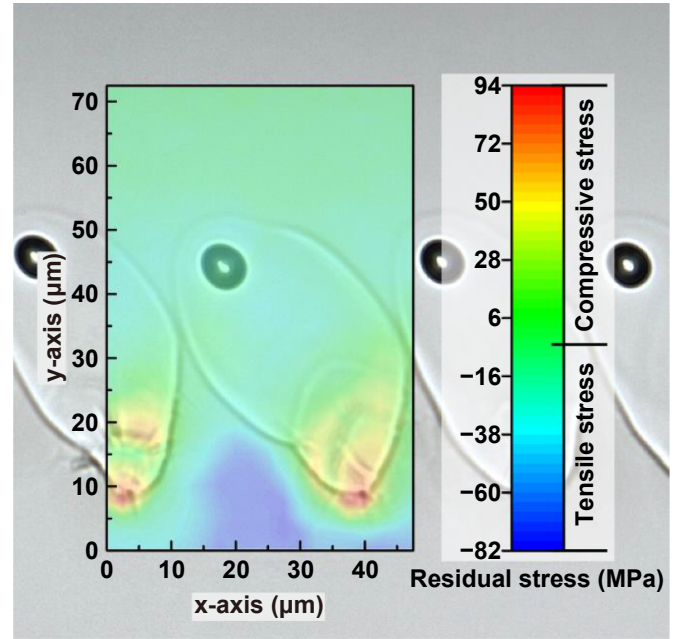

Figure 14. Calculation of the residual stress for a modified zone inscribed with an average power of 3 W, a repetition rate of 2 MHz and a feeding speed of 200 mm s^{-1}. The residual stress is obtained by combining the Brillouin shift of figure 12 with the σ-parameter of figure 9 by using equation (8). The calculated residual stress is color coded and overlaid with an optical image of identical scale.

4. Conclusion

In our work, fused silica was prepared at different fictive temperatures, similar to cooling rates, by using a conventional annealing method. Different observables obtained from inelastic light scattering (optical and acoustic vibrations of the glass network) were correlated to the T_f and calibration curves. Concerning our experimental study, the observed T_f range reported in the literature was expanded to lower T_f values. This provides a more reliable extrapolation for all the observables studied. The expanded range of T_f shows a slightly different behavior compared to literature.

A USP laser modified zone in fused silica was produced and mapped with high spatial resolution by Raman and Brillouin spectroscopy. The mapping of the modified zone provides a detailed view of the T_f distribution within the modified zone. We observed, by the Raman signal, a higher T_f in the center of the modified zone indicating a higher cooling rate. Using the USP laser, it was possible to generate higher T_f compared to our conventional annealing method. The results of the σ-parameter and the D_2 *area* were found to be very suitable for a local mapping of the T_f across the USP laser modified zone. The Raman *main band position* by itself was less accurate. Moreover, the σ-parameter and the D_2 *area* only show the response to changes in T_f and are not influenced by residual stress. The observation of the Brillouin signal shows additional effects besides the T_f due to residual stress. However, if the residual stresses are low enough (<2 GPa) the combination of the Raman signal (σ-parameter) and the Brillouin shift can be used to separate and quantify the influence of residual stress

on the glass network. The measured cooling rate and residual stress in our study can be used to validate future simulations of the GBCZ and USP laser modified zones in fused silica.

Acknowledgments

ORCID iDs

Michael Bergler ⓘ https://orcid.org/0000-0002-9910-8649
Kristian Cvecek ⓘ https://orcid.org/0000-0001-7417-4829

References

[1] Mishchik K, Chassagne B, Javaux-Léger C, Hönninger C, Mottay E, Kling R and Lopez J 2016 Dash line glass- and sapphire-cutting with high power USP laser *Proc. SPIE* **9740** 97400W

[2] Miyamoto I, Cvecek K, Okamoto Y, Bechthold P and Schmidt M 2009 Laser-matter interaction in fusion welding of fused silica using ultrashort pulse lasers *Proc. LAMP 2009, 5th Int. Congress on Laser Advanced Materials Processing* p 108

[3] Alexeev I, Cvecek K, Miyamoto I and Schmidt M 2010 Ultrafast laser processing of transparent media–glass welding *Proc. LEF 2010, Laser in der Elektronikproduktion & Feinwerktechnik (Laser in Electronic Production and Precision Mechanics)* (Fürth, Germany) pp 125–37

[4] Diels J C and Rudolph W 2006 *Ultrashort Laser Pulse Phenomena. Fundamentals, Techniques, and Applications on a Femtosecond Time Scale* 2nd edn (New York: Academic)

[5] Hernandez-Rueda J, Clarijs J, Van Oosten D and Krol D M 2017 The influence of femtosecond laser wavelength on waveguide fabrication inside fused silica *Appl. Phys. Lett.* **110** 161109

[6] Weingarten C, Schmickler A, Willenborg E, Wissenbach K and Poprawe R 2017 Laser polishing and laser shape correction of optical glass *J. Laser Appl.* **29** 011702

[7] Weingarten C, Steenhusen S, Hermans M, Willenborg E and Schleifenbaum J H 2017 Laser polishing and 2PP structuring of inside microfluidic channels in fused silica *Microfluid. Nanofluid.* **21** 165

[8] Schuöcker D and Schuöcker G D 2014 *Advanced Laser Materials Processing* (Foster City, CA: OMICS International) (https://doi.org/10.4172/ 978-1-63278-027-0-028)

[9] Zimmermann F, Lancry M, Plech A, Richter S, Ullsperger T, Poumellec B, Tünnermann A and Nolte S 2017 Ultrashort pulse laser processing of silica at high repetition rates—from network change to residual strain *Int. J. Appl. Glass Sci.* **8** 233–8

[10] Li C Y and Tomozawa M 2012 Fictive temperature and fictive pressure measurement of silica glasses using FTIR method: for thick samples and samples containing Si–H *J. Non-Cryst. Solids* **358** 3365–71

[11] Sonneville C, Mermet A, Champagnon B, Martinet C, Margueritat J, De Ligny D, Deschamps T and Balima F 2012 Progressive transformations of silica glass upon densification *J. Chem. Phys.* **137** 124505

[12] Deschamps T, Kassir-Bodon A, Sonneville C, Margueritat J, Martinet C, De Ligny D, Mermet A and Champagnon B 2013 Permanent densification of compressed silica glass: a raman-density calibration curve *J. Phys.: Condens. Matter* **25** 025402

[13] Deschamps T, Margueritat J, Martinet C, Mermet A and Champagnon B 2015 Elastic moduli of permanently densified silica glasses *Sci. Rep.* **4** 7193

[14] Badrinarayanan P, Zheng W, Li Q X and Simon S L 2007 The glass transition temperature versus the fictive temperature *J. Non-Cryst. Solids* **353** 2603–12

[15] Caponi S, Fontana A, Mattarelli M, Montagna M and Rossi F 2007 The influence of the fictive temperature and the OH content on the dynamical properties of vitreous silica: comparison of Raman, Brillouin, and neutron scattering spectra *J. Phys.: Condens. Matter* **19** 205149

[16] Shelby J E 2005 *Introduction to Glass Science and Technology* 2nd edn (Cambridge: Royal Society of Chemistry) (https://doi.org/10.1039/9781847551160)

[17] Dingwell D B and Webb S L 1990 Relaxation in silicate melts *Eur. J. Mineral.* **2** 427–51

[18] Jochs W W, Hoffmann H J and Neuroth N M 1988 The effects of thermal treatment below the glass transition temperature on the refractive index of optical glass *J. Non-Cryst. Solids* **102** 255–8

[19] Levelut C, Le Parc R, Faivre A and Champagnon B 2006 Influence of thermal history on the structure and properties of silicate glasses *J. Non-Cryst. Solids* **352** 4495–9

[20] Lancry M, Régnier E and Poumellec B 2012 Fictive temperature in silica-based glasses and its application to optical fiber manufacturing *Prog. Mater. Sci.* **57** 63–94

[21] Elektrisch geschmolzenes Quarzglas EN08 2019 (available at: http://www.g-v-b.de/File/quarzplatten_d1.pdf)

[22] Moynihan C T, Easteal A J, Wilder J and Tucker J 1974 Dependence of the glass transition temperature on heating and cooling rate *J. Phys. Chem.* **78** 2673–7

[23] Yue Y Z, Von Der Ohe R and Jensen S L 2004 Fictive temperature, cooling rate, and viscosity of glasses *J. Chem. Phys.* **120** 8053–9

[24] Yue Y Z 2008 Characteristic temperatures of enthalpy relaxation in glass *J. Non-Cryst. Solids* **354** 1112–8

[25] Veber A, Cicconi M R, Reinfelder H and De Ligny D 2018 Combined Differential scanning calorimetry, Raman and Brillouin spectroscopies: a multiscale approach for materials investigation *Anal. Chim. Acta* **998** 37–44

[26] Boizot B, Agnello S, Reynard B, Boscaino R and Petite G 2003 Raman spectroscopy study of β-irradiated silica glass *J. Non-Cryst. Solids* **325** 22–28

[27] Hehlen B 2010 Inter-tetrahedra bond angle of permanently densified silicas extracted from their Raman spectra *J. Phys.: Condens. Matter* **22** 025401

[28] Galeener F L 1982 Planar rings in glasses *Solid State Commun* **44** 1037–40

[29] Gavenda T, Gedeon O and Jurek K 2015 Irradiation induced densification and its correlation with three-membered rings in vitreous silica *J. Non-Cryst. Solids* **425** 61–66

[30] Gavenda T, Gedeon O and Jurek K 2017 Structural and volume changes and their correlation in electron irradiated alkali silicate glasses *Nucl. Instrum. Methods Phys. Res. Sect.* B **397** 15–25

[31] Saavedra R Saavedra R, León M, Martin P, Jiménez-Rey D, Vila R, Girard S, Boukenter A and Ouerdane Y 2014

Raman measurements in silica glasses irradiated with energetic ions *AIP Proc.* **1624** 118–24

[32] Cvecek K, Alexeev I, Miyamoto I and Schmidt M 2010 Defect formation in glass welding by means of ultra short laser pulses *Phys. Procedia.* **5** 495–502

[33] Malitson I H 1965 Interspecimen comparison of the refractive index of fused silica *J. Opt. Soc. Am.* **55** 1205–9

[34] Miyamoto I, Cvecek K, Okamoto Y and Schmidt M 2014 Internal modification of glass by ultrashort laser pulse and its application to microwelding *Appl. Phys.* A **114** 187–208

[35] Miyamoto I, Cvecek K and Schmidt M 2013 Crack-free conditions in welding of glass by ultrashort laser pulse *Opt. Express* **21** 14291–302

[36] Cvecek K, Miyamoto I and Schmidt M 2014 Gas bubble formation in fused silica generated by ultra-short laser pulses *Opt. Express* **22** 15877–93

[37] Tomozawa M, Koike A and Ryu S R 2008 Exponential structural relaxation of a high purity silica glass *J. Non-Cryst. Solids* **354** 4685–90

[38] Martinet C, Martinez V, Coussa C, Champagnon B and Tomozawa M 2008 Radial distribution of the fictive temperature in pure silica optical fibers by micro-Raman spectroscopy *J. Appl. Phys.* **103** 083506

[39] Le Parc R, Levelut C, Pelous J, Martinez V and Champagnon B 2006 Influence of fictive temperature and composition of silica glass on anomalous elastic behaviour *J. Phys.: Condens. Matter* **18** 7507–27

[40] Miyamoto I, Okamoto Y, Tanabe R, Ito Y, Cvecek K and Schmidt M 2016 Mechanism of dynamic plasma motion in internal modification of glass by fs-laser pulses at high pulse repetition rate *Opt. Express* **24** 25718–31

[41] Miyamoto I, Okamoto Y, Tanabe R, Ito Y, Schmidt M, Merklein M and Vollertsen F 2014 Characterization of plasma in microwelding of glass using ultrashort laser pulse at high pulse repetition rates *Phys. Proc.* **56** 973–82

[42] Peng Y L, Agarwal A, Tomozawa M and Blanchet T A 1997 Radial distribution of fictive temperatures in silica optical fibers *J. Non-Cryst. Solids* **217** 272–7

[43] Deschamps T, Martinet C, De Ligny D and Champagnon B 2009 Elastic anomalous behavior of silica glass under high-pressure: in-situ Raman study *J. Non-Cryst. Solids* **355** 1095–8

[44] Cvecek K, Miyamoto I, Heberle J, Bergler M, De Ligny D and Schmidt M 2018 Analysis of shockwave formation in glass welding by ultra-short pulses *Procedia CIRP* **74** 339–43

[45] Maugeri E A, Peuget S, Staicu D, Zappia A, Jegou C and Wiss T 2012 Calorimetric study of glass structure modification induced by α decay *J. Am. Ceram. Soc.* **95** 2869–75

[46] Weber R, Giedl-Wagner R, Förster D J, Pauli A, Graf T and Balmer J E 2019 Expected X-ray dose rates resulting from industrial ultrafast laser applications *Appl. Phys.* A **125** 635